Materials Advances

Accepted Manuscript

This article can be cited before page numbers have been issued, to do this please use: Q. ul Hassan, S. A. A. Shah, M. U. Salman, M. Luqman, M. Mehak, M. J. Iqbal and S. Atiq, *Mater. Adv.*, 2026, DOI: 10.1039/D6MA00053C.

View Article Online
DOI: 10.1039/D6MA00053C

Tuning the thicknesses, density of states, electron affinities of layers in perovskite-based solar cells for green energy solutions

Qayyum ul Hassan, Syed Aqib Abbas Shah, Muhammad Umar Salman, Muhammad Luqman, Muhammad Mehak, Muhammad Javaid Iqbal, Shahid Atiq*

Centre of Excellence in Solid State Physics, University of the Punjab, Lahore-54590, Pakistan

Abstract

The global demand for energy has increased rapidly, highlighting the urgent need for sustainable and renewable energy solutions. Among renewable sources, solar energy has attracted significant attention, with perovskite solar cells (PSCs) emerging as a promising technology. In this context, $BiFeO_3$ (BFO) has gained interest as an absorber material due to its robust remanent polarization and room-temperature ferroelectricity, which eliminates the need for a traditional p-n junction. This study investigates a 3D ZnO/BFO/Spiro-OMeTAD PSC architecture using COMSOL Multiphysics simulations. Device performance is influenced by electron affinity (EA) and density of states (DOS) in BFO, with efficiency varying from 8.96% to 11.28% as these parameters change. Optimization of photovoltaic parameters yields a maximum efficiency of ~11.83%, short-circuit current density of ~10.12 mA/cm^2, open-circuit voltage of ~1.8 V, and fill factor of ~64.91%. The presented simulation framework provides reproducible insights into material and interface optimization, bridging numerical modeling with experimental trends. These findings offer practical guidance for designing high-performance PSCs and advancing next-generation photovoltaic devices.

Keywords: COMSOL Multiphysics; Semiconductor; Green energy; Perovskite solar cells; Photovoltaic; Renewable energy

***Corresponding Author:** Shahid Atiq (satiq.cssp@pu.edu.pk)

View Article Online
DOI: 10.1039/D6MA00053C

1. Introduction

Renewable energy is being recognized as a top priority due to the world's growing energy needs (which have increased over the past year by 1.7%) and the pressing need to reduce the release of CO_2 (53.0 Gt) from traditional resources like coal and gasoline [1–3]. In order to meet this rising energy demand, solar power could act as a suitable resource alongside various renewable energy sources, and innovations regarding photovoltaic (PV) technologies have been greatly accelerated by the growing need for energy from renewable sources [4, 5]. The development of non-traditional photovoltaic techniques, such as lead-halide perovskite (LHPs), kieserite's, organic material photovoltaics, and oxide-driven solar cells (SCs), has received a lot of attention over the past decade. The investigation of lead-free (Pb-free) particularly environmentally harmless absorber materials has been spurred by worries about toxicity as well as longevity, even though LHPs have shown impressive efficiency [6]. In this regard, oxide- and ferroelectric-derived SCs have become attractive options because of their environmentally friendly nature, chemical stabilization, and stability for scalable manufacturing processes [7].

Probably the most promising of these developments, perovskite solar cells (PSCs) stand out because of their ferroelectric characteristics, significant dielectric constant (~3.1 to ~7.1), low bonding excitation energy, and large absorption coefficient (10^4 –10^5 cm^{-1} at about 400 nm) [8–11]. These distinctive characteristics provide perovskite materials with the potential for commercialization and feasible manufacturing in large quantities, allowing them to produce remarkable PV performance [12]. With the goal to achieving the best possible device efficiency along with stability, recent developments in PSCs have highlighted the key impact that material choice plays in the electron transport layer (ETL), PVK absorption layer, as well as hole transport layer (HTL). Therefore, material tuning has emerged as a robust and rapidly emerging field of study [13].

In addition to the ETL materials, zinc oxide (ZnO) is a great ETL option because it is a semiconductor having a wide bandgap ~2.5 eV (at ambient temperature), high affinity for electrons, and an exciton binding energies of 60 meV [14]. Because of its great transparency and elevated electron mobility, which may help in electron transport and lessen unwanted recombination losses, ZnO stands out among the most promising ETL options [15]. For the sake

View Article Online
DOI: 10.1039/D6MA00053C

of PVK absorber layer, $BiFeO_3$ (BFO) has become a very attractive material for PV applications because of its unique combination of ferroelectric and antiferromagnetic characteristics [16, 17]. BFO has garnered significant interest among Pb-free oxides absorbers because of its large absorption coefficient (~1.88×10^5 cm^{-1}), low optical band-gap (E_g ~2.5 eV), and inherent ferroelectric polarization (up to 100 $\mu C/cm^2$) that can provide effective separation of charges beyond traditional p-n junction methods [18, 19]. BFO provides improved photogeneration while maintaining superior thermal and chemical stability, compared to numerous wide E_g oxide materials that have inadequate absorption within the visible spectrum [20]. BFO showed efficiencies of up to 11.83%, whereas other ferroelectric materials have shown efficiencies of about 0.1% [21]. With a rhombohedral shape, BFO also has high Curie and Néel temperatures of around 1103 K and 643 K, respectively [22]. Numerous investigations show that the BFO is a p-type material since its Fermi level lies close to its valence band [23]. The HTL has become equally critical since it controls effective hole collection and transport. Spiro-OMeTAD, a popular HTL material, exhibits outstanding performance because of its exceptional hole mobility, superior thin film formation, and stable operation, and because of its coherence with BFO, recombination losses are decreased and charge transport ability is increased [24–27]. In contrast to previous oxide and chalcogenide absorbing material designs, the 3D ZnO/BFO/spiro-OMeTAD coupling thus serves as a dynamically balanced configuration that combines stability, Pb-free architecture, and ferroelectric-aided carrier kinetics.

Making use of these traits, Wani, *et al*. (2024) claimed that short-circuit current density (J_{sc}), V_{oc}, fill factor (FF), and efficiency outcomes for the ITO/ZnO-uc/BFO/AI architecture were found to be 4.7 mA/cm^2, 0.89 V, 53%, and 2.21% respectively [28]. Likewise, Afzal *et al*. (2020) investigated the ITO/Graphene/ZnO/BFO/Graphene design, achieving an efficiency of 7.8% along with V_{oc}~0.6 V and J_{sc}~13.155 mA/cm^2 [29]. Similarly, Raj *et al.* (2024) reported that the FTO/ZnO/BFO/Spiro-OMeTAD/Au solar cell exhibited a V_{oc} ~ 0.79 V, J_{sc} ~ 8.35 mA/cm^2, FF ~ 29.10%, and an efficiency of 1.92% [30]. Furthermore, innovation was shown by Mahammedi *et al*. (2024), who tuned the bandgap (E_g) of Bi_2FeCrO_6 between 1.4 eV and 2.4 eV using Fe/Cr cationic ordering, reaching an efficiency of 7.3% with FF~53.7%, J_{sc}~12.15 mA/cm^2, and V_{oc} ~1.12 V [31].

View Article Online
DOI: 10.1039/D6MA00053C

Given these encouraging characteristics, the photovoltaic potential of 3D ZnO/BFO/Spiro-OMeTAD PSCs is still constrained by a lack of knowledge regarding active layer thickness tuning, interfacial band alignment, as well as the impact of DOS upon transport of carrier's particularly recombination. In this research, a comprehensive numerical study of 3D ZnO/BFO/Spiro-OMeTAD SCs in this study, with an emphasis on the combined impacts of DOS engineering, EA adjustment, and absorber layer thickness on performance. In contrast to earlier research that mostly reports isolated parameter alterations or experimental efficiency, this work offers a cohesive and physically oriented analysis connecting material attributes to photovoltaic parameters. Hence, these findings provide predictive design guidance to support experimental attempts to optimize Pb-free BFO-based PSCs. In this study, the 3D ZnO/BFO/Spiro-OMeTAD framework in order to investigate a totally toxic-free, thermally resistant, and readily accessible and to comprehend the parameters that currently limit its performance.

2. Theoretical framework

The 3D ZnO/BFO/Spiro-OMeTAD solar cells (SCs) operates as a multi-layered system, meticulously designed for optimal photon capture and efficient charge transport. Here, ZnO works as electron transport layer (ETL), BFO takes on the role of the primary photon-absorbing material, and Spiro-OMeTAD serves as the dedicated conduit for hole transport. The theoretical framework intertwines optical dynamics, charge kinetics, interfacial phenomena, and material-specific parameters of absorber layer, including EA, DOS, thickness, and Fermi-Dirac principles. Therefore, three fundamentally important differential equations the Poisson's equation (Eq. 1), continuity principle (Eq. 2), and the transport principle (Eq. 3) form the basis of simulation, enabling an in-depth investigation of the function of solar cells. In photovoltaic cells, the carrier's dynamics is controlled by transport formulas. Whereas, Poisson's equation describes how charges are distributed along with electric field, and continuity expression deals with recombination as well as carrier's production.

$$\frac{\partial^2\varphi}{\partial^2 x} = -\frac{\partial E}{\partial x} = -\frac{q}{\varepsilon_s}[p - n + N_D(x) - N_A(x) \pm N_{def}(x)] \quad (1)$$

$$\frac{\partial n,p}{\partial t} = \frac{1\partial J_n}{q\,\partial x} + (G_n - R_n) + \frac{1\partial J_p}{q\,\partial x} + (G_p - R_p) \quad (2)$$

View Article Online
DOI: 10.1039/D6MA00053C

$$J_{n,p} = nq\mu_n E + qDn\frac{\partial n}{\partial x} + nq\mu_p E + qDp\frac{\partial p}{\partial x} \quad (3)$$

Here, in Eqs. 1-3, φ symbolizes the electrostatic potential, ε_s permittivity of material, while n, p are free electron/hole densities, N_D & N_A are donor and acceptor impurities, N_{def} is defects density, electron/hole current density is represented by $J_{n,p}$, q is charge, and μ_{np} is the charge dynamics. The aforementioned mathematical equations were successfully solved regarding steady-state settings using COMSOL Multiphysics semiconductors module of the program. The conducting electrodes were subjected to satisfy boundary conditions that corresponded to ohmic especially selective connections. All of these equations directly affects the computed current-voltage properties, such as band bending as well as inner electric fields are governed by Poisson's equations, carrier's harvesting under illumination was computed by the continuity mathematical models, while non-radiative impacts are controlled by corresponding DOS recombination factors. Therefore, the quantitative assessment of material factor's effects on quantifiable photovoltaic outcomes is made possible by this coupled approach [32 – 36].

The Recombination processes play a key role in determining how efficient a device is, and radiative recombination occurs by photon emission, whereas, Shockley-Read-Hall (SRH) recombination takes into account trap states inside the E_g. The continuity models are modified to include such recombination mechanisms for the purpose to account for the dynamics underlying carrier loss. The SRH recombination process reveals the pathway through which charge carriers annihilate via intermediary defects states or traps embedded in a semiconductor's E_g. These impurity or structural anomaly-induced traps serve as carriers dynamics impede. The SRH recombination has a significant impact on semiconductor device performance, particularly when defect-driven mechanisms take center stage or simply pristine substance is not available [37]. The SRH recombination is give as (Eqs. 4 and 5) [38].

$$R_{RSH} = \frac{np - n_i p_i}{\tau_n(p+p_1) + \tau_{p(n+n_1)}} \quad (4)$$

$$\tau_{n,p} = \frac{1}{N_t V_{th} \sigma_{n,p}} \quad (5)$$

Here, in Eqs. 4 and 5, N_t shows defect density, V_{th} denotes the thermal velocities of electron and holes (e/h), $\sigma_{n,p}$ symbolizes the capture cross-sectional areas of electrons and holes, and $\tau_{n,p}$

View Article Online
DOI: 10.1039/D6MA00053C

represents the carrier's lifetimes of electrons and holes. The FF controls how a SCs behaves overall, whereas efficiency is defined simply the relation regarding its output power with input power. The FF ranges from 0 to 1, with a closer value to 1 indicating improved SCs performance [39, 40]. The values of these two quantities can be acquired from the following relations (Eqs. 6 and 7).

$$FF = \frac{J_{max} \times V_{max}}{J_{sc} \times V_{oc}} \tag{6}$$

$$PCE = \frac{V_{oc} \times J_{sc} \times FF}{P_{in}} \tag{7}$$

Overall computational procedure used in this investigation is summed into the format that follows to guarantee reproducibility for the final outcomes given. Initially, device design along with thickness of layers were determined using studies on BOF-related heterojunctions that were published. Under AM1.5G light, photo generation was computed utilizing BFO's wavelength-based absorption characteristic. In order to simulate carrier's transport, Poisson's differential equation was systematically solved coupled with e/h continuity principle, adding SRH recombination according to distributed DOS additionally drift diffusion transportation. Additionally, a distinct correlation connecting specific physical mechanism as well as device operational parameters was made possible by methodically varying each material properties one at each step while maintaining the same values for every other. Table 1 provides the layer-specific optimize parameters, sourced individually from the relevant studies, with simulations conducted at a temperature of 293 K.

3. Results and discussion

3.1 Energy levels schematic diagram

Fig. 1(a) depicts a 3D ZnO/BFO/Spiro-OMeTAD SCs with ZnO acting as ETL, BFO's being the incident photons absorbing perovskite, and Spiro-OMeTAD gathering holes for effective separation of charges and transportation. Fig. 1(b) shows that the BFO's layer absorbs photons to create electron-hole pairs, which are then transmitted to the ETL and gather at its front contact. Whereas holes are moved to the rear contact via HTL, this process demonstrates energy-level proper alignment as well as transportation of charges in SCs. In which crossed arrows guarantee

View Article Online
DOI: 10.1039/D6MA00053C

selective charge transfer and lower recombination losses by indicating electrons that unable to approach the HTL as well as holes that are kept from doing so. Fig. 1(c) illustrates optical staggered band configuration that guarantees efficient charge carrier segregation as well as transport across optical energy band structure of 3D ZnO/BFO/Spiro-OMeTAD SCs. Its Quasi-Fermi states regarding electrons (E_{fn}) as well as holes (E_{fp}) show the mobility of charges. Whereas the conduction band edge (E_c) and also valence band edge (E_v) show the alignment throughout its layers structure. Staggered alignment minimizes recombination, as well as carrier's backflow and maximize performance as electrons flow towards the ETL while holes are guided towards HTL [41].

3.2 Solar irradiance and generation rate

Fig. 2(a) reveals the solar irradiance at different wavelengths assuming as the light source, A.M 1.5 G, within the visible region (400-700 nm), attain a luminosity peak ~1.6 W/m^2/nm around 460 nm, indicating the efficient availability of visible light to generate charge carriers. Irradiance decrease after 1000 nm, indicating insignificant solar energy over the infrared spectrum. Fig. 2(b) shows in what way extinction coefficient (k) as well as refractive index (n) change with wavelength; n value is larger in the UV region while it steadily decreases for both visible as well IR zones. This suggests improved light trapping and decreased reflection, especially in the UV-visible range. On the other hand, because of strong electronic transitions, k is high for the UV, decreases during the visible region and minimal for the IR, which remains consistent for the cell's absorbing properties. Fig. 2(c) illustrates, light absorption falloffs deeper within an absorber layer, the electron/hole (e/h) pair creation rate drops exponentially by increasing arc length, observing the law of Beer-Lambert. Fig. 2(d) shows that due to lower concentration of carriers close to the surface, SRH recombination pattern starts at lower arc length and minor increase in recombination occurs by increasing carrier's concentration as arc length increases. Following this, as carriers start to diffuse farther within the absorber layer, lowering localized recombination, this rate momentarily decreases [42].

3.3 Device construction layout

The 3D ZnO/BFO/Spiro-OMeTAD PSCs was simulated in COMSOL Multiphysics, the process begins with specifying actual geometry, in which ZnO (ETL), BFO (PVK), and Spiro

View Article Online
DOI: 10.1039/D6MA00053C

(HTL) layers are precisely denoted in 3D device layout and layer's set-up. The next step is material choice, where each individual layer is given the optimal electrical along with optical characteristics. After that, for the sake of simultaneous results, a multiphysics component is chosen to group semiconductor with optical physical phenomena. Following linked governing formulas was processed numerically right through the computing phase, in addition steady-state computations under illumination along with bias settings obtained by the stationary investigation. Soon after that, the domain was discretized via meshing, with improved elements at key contacts to achieve numerical correctness. Moreover, convergence analysis works out to verify mesh validity and solution consistency, confirming the accuracy of its results. Later this, the model undergoes optimization with key factors like thickness of layers or DOS being methodically changed to improve device function. Eventually, the optimal data is obtained as photovoltaic performance measurements especially J-V characteristics of device. Fig. 2(e) demonstrates the schematic diagram and provides a procedural guidance for using COMSOL Multiphysics program to replicate this structure.

The optical input for the simulation is the standard AM 1.5 solar spectrum, which is used as the illumination source to evaluate realistic photovoltaic operation under one-sun conditions. At the material level, all layer specific parameters including band gap, electron affinity, relative permittivity, carrier mobilities, effective density of states, and recombination parameters are taken as direct inputs, as summarized in Table 1. These parameters define the physical behavior of each functional layer in the device stack and form the basis of the numerical model.

Several physical and numerical assumptions are adopted to make the problem well defined and computationally stable. The device is assumed to be directly exposed to the environment, meaning to encapsulation or top glass layer is considered, so optical losses due to external shielding are neglected. All interfaces are assumed to be homogeneous, with abrupt and ideal transitions between adjacent layers, without interfacial roughness or compositional grading. Carrier transport is modeled by solving the coupled Poisson and continuity equations for both electrons and holes. Fermi-Dirac statistics are employed instead of Maxwell-Boltzmann statics to obtain more accurate carrier distributions, particularly under high doping and strong electric field conditions. The interface continuation parameter is assumed to be ideal and set equal to unity, implying perfect electrical continuity across interfaces. No coupling between doping profiles and trap states is

View Article Online
DOI: 10.1039/D6MA00053C

assumed and trap assisted tunneling is neglected. Tunneling mechanisms are therefore disabled in the model. For numerical discretization, a finite volume approach is adopted with constant shape functions, ensuring charge conservation and numerical robustness. In heterojunction regions, quasi-Fermi levels are assumed to describe carrier transport under non-equilibrium conditions. Finally, the metal contacts are modeled as pure ohmic contacts, neglecting contact resistance and Schottky barrier effects, in order to focus on intrinsic device physics.

3.4 Effect of BFO's thickness variation on PV performance

The absorbing layer as well as its thickness in solar cell plays a pivotal role in output performance. Fig. 3(a) shows that schematic illustration to probe the effect of absorbing layer and its thickness, illustrates photo-generated carriers are created, separated, and transported; elevated thickness causes recombination (R_{ETL}, R_{HTL}), that lowers efficiency. Fig. 3(b) & (c) illustrate improved light absorption as well as effective charge transfer in 3D ZnO/BFO/Spiro-OMeTAD SCs, and provide the J-V and P-V characteristics. Power output drops as the BFO's thickness increases, it peaks at 108.14 W (300 nm) and then gradually drops towards 40.24 W (1550 nm) as a result of recombination losses. Fig. 3(d) depicts variation in J_{sc}, V_{oc}, and P_{max}: here J_{sc} rises from 9.92 mA/cm^2 (at 300 nm) as thickness of the active layer increases, reaching its highest value of ~10.35 mA/cm^2 (at 800 nm). Beyond this point, it levels off at approximately ~10.32 mA/cm^2 within the range of 1050-1300 nm, eventually falls to 9.30 mA/cm^2 at 1550 nm, signifying that optimal thickness for achieving maximum J_{sc}. It also indicates that enhanced photon absorption along with energy alignment cause V_{oc} to increase from 1.7 V (at 300 nm) to 1.8 V (at 550 nm–800 nm). However, after 800 nm, V_{oc} marginally drops and stabilize around 1.7 V for thicknesses reaching 1550 nm, suggesting saturation effect predominates at greater thicknesses. Yet, P_{max} stays relatively stable between 108.1 W and 104.7 W for thicknesses between 300 and 800 nm, then gradually decreases to 98.8 W (at 1300 nm) due to reduced charge collection effectiveness. P_{max} sharply decreases to 40.2 W (at 1550 nm), most likely caused by optical loss outweighing the benefits of increased thicknesses. Fig. 3(e) shows %FF and %efficiency behavior which reflects when resistive effect increases, the FF decreases from 64.11% (at 300 nm) to an extent of 56.20–57.28% for (1050 –1300 nm), suggesting a stable but decreasing performance. The sharp decline in FF to 25.4% (at 1550 nm) is probably caused by substantial recombination and ineffective carrier's transportation. This shows steady performance with minimal efficiency losses resulting

View Article Online
DOI: 10.1039/D6MA00053C

from increased thickness, beginning at 10.81% (at 300 nm) and decrease to 9.88% (at 1300 nm). At 1550 nm, on the other hand, efficiency declines precipitously to 4.02%, most likely as a result of reduced carriers transport efficiency along with significant optical losses [43]. Table 2 provides the effect of BFO's thickness variation on output characteristics of photovoltaic performance of propose SCs configuration.

3.5 Effect of ZnO's thickness variation on PV performance

Fig. 4(a) lays out the study associated with ZnO's thickness, showing that an ideal thickness of 40 nm at which J_{sc} (~8.83 mA/cm^2) is maximum. As thickness increases (10 – 40 nm) V_{oc} steadily increases from 2.02 to 2.03 V and reaches an optimum value of ~2.23 V (at 50 nm), hence after this ideal thickness (50 nm), V_{oc} starts decreasing slowly to ~2.03 V (at 60 nm). This may be due to probably by insufficient light absorption as well as high series resistance (R_S) inside the device architecture. Fig. 4(b) shows that power output measurement for different ZnO's thicknesses reveals a gradual increase from 117.85 W (at 10 nm) to 118.12 W (at 60 nm), thinner layers (10-50 nm) harvest relative lower power output. It is due to the lower charge transfer and poor light harvesting effect, and gradually increase in thickness above 50 nm, improves light absorption which ultimately enhances power output. Fig. 4(c) exhibits J_{sc}, V_{oc}, and P_{max} in which J_{sc} starts rising from 8.82 mA/cm^2 (at 10 nm) until a maximum of 8.83 mA/cm^2 (at 40 nm) and remain steady towards 60 nm as a result of excellent light absorption, and charge collecting ability. Furthermore, V_{oc} increases as ZnO's thickness increases; it starts from 2.02 V (at 10 nm), and attains a maximum of 2.23 V (at 50 nm), and then drops gradually to 2.03 V after the ideal thickness of 50 nm. The main cause of this behavior due to increase in R_S and reduction in electric field, each of which makes it more difficult for charges to separate and move through the device effectively. But, P_{max} increases as ZnO's thickness increases, reaching to maximum power peak ~118.12 W at 60 nm which is due to the higher light absorption, optimum transport of charges, and low resistance. Fig. 4(d) illustrates %FF and %efficiency trend, FF gets improved as ZnO's thickness increases (10–30 nm) due to improved charge extraction, yet it gets a little lower after 30 nm because of increase in resistance. On the contrary, as ZnO's thickness increases, the efficiency rises from ~11.78% (at 10 nm) to ~11.82 % (at 60 nm) because of increased in absorption, charge transport strength, and reduced R_S, therefor thicker ZnO's layer (60 nm) yields

View Article Online
DOI: 10.1039/D6MA00053C

the optimum efficiency [44]. Table 3 provides the effect of ZnO's thickness variation on output characteristics of PV performance of proposed SCs configuration.

3.6 Effect of BFO's DOS variations on PV performance

Fig. 5(a) illustrating the dynamics variation in the DOS within the BFO's layer of the 3D ZnO/BFO/Spiro-OMeTAD PSCs, and provides the J-V characteristic. However, a fascinating interplay emerges in the V_{oc}, which exhibits a significant decline as DOS escalates at $N_{c/v}= 1\times10^{16}$ cm^{-3}, the V_{oc} reaches an optimal magnitude of 1.8 V, after this it gradually decreases to 1.5 V at 1×10^{20} cm^{-3}. This compelling behavior highlights the profound impact of increased DOS, which intensifies recombination losses, slightly decreasing V_{oc} whereas J_{sc} persistently holds its ground. Fig. 5(b) shows that with rising DOS, the power output declines from ~118.28 W to ~89.93 W, as V_{oc} reduces from 1.8 V to 1.5 V, owing to amplified recombination and resistive losses obstructing carrier's transportation. Fig. 5(c) shows variation in J_{sc}, V_{oc}, and P_{max} which reveals that the constancy of J_{sc} (~10.123 mA/cm^2) with in the DOS span of 1×10^{16}–1×10^{19} cm^{-3} suggests that photonic generation and carrier's extraction, are mainly tolerant to DOS fluctuations in this domain. Because of increased carrier recombination liked to hither DOS, the V_{oc} gradually drops. As a result of higher non-radiative expenses and shorter carrier lifetime, the P_{max} and FF decrease. However, a slight rise in J_{sc} (~10.124 mA/cm^2) at 1×10^{20} cm^{-3} corresponds to computing tolerance and is not indicative of some sort of fundamental transport boots, but rather of small shift towards the band-edge carrier's density . Consequently, this demonstrates that DOS modifications mostly affects the quasi-Fermi levels splitting along with recombination dynamics instead of J_{sc} generation process. However, V_{oc} drops primarily because of the enhanced non-radiative recombination caused by an increase in DOS, leading to greater energy dissipation, and limiting the achievable voltage. This effect is commonly observed in PSCs in which large number of states trap charge carriers, reducing the separation of quasi-Fermi levels. This further indicates that as DOS rises 1×10^{16}–1×10^{20} cm^{-3}, P_{max} falls suggesting that higher DOS results in increased recombination and lower power generation. Fig. 5(d) shows variation in %FF and %efficiency, FF marginally rises at 1×10^{17} cm^{-3} because of better carrier's transport, yet it falls after that due to higher DOS which leads to more non-radiative recombination that impairs productivity. Correspondingly, efficiency falls from ~11.83% (at 1×10^{16} cm^{-3}) to 8.99 % at 1×10^{20} cm^{-3} this is due to the effect that the increase in DOS provides more trapping states, which ultimately speeds

View Article Online
DOI: 10.1039/D6MA00053C

up recombination, and shortens carrier's lifetime. [45]. Table 4 provides the output characteristics of proposed SCs configuration at varying DOS of BFO layer.

3.7 Effect of electron affinity (EA) of absorbing layer on PV performance

Electron affinity is a key parameter governing energy band alignment at the interfaces between the absorber and charge transport layers in photovoltaic devices. Proper electron affinity alignment controls the conduction and valence band offsets, enabling efficient electron extraction to the electron transport layer and hole transport layer. Favorable band offsets reduce interfacial energy barriers and suppress carrier recombination losses. As a result, charge separation and transport are enhanced, leading to improved short-circuit current density and open-circuit voltage. Consequently, optimized electron affinity contributes directly to the higher overall power conversion efficiency.

Fig. 6(a) illustrates the J-V curve and Fig. 6(b) shows the P-V characteristics at different electron affinities of absorbing layer and the P_{max} value increased with BFO electron affinities due to maximum generation of charge carriers like electrons and holes and lower recombination. Fig. 6(c) shows the variation in J_{sc}, V_{oc}, and P_{max} at same range of electron affinities, where a slight change in J_{sc} happens as EA decreases, beyond the point at 2.5 eV it stabilized at 8.82 mA/cm^2 for greater EA (2.6–2.8 eV) due to maximum recombination occurs of charge carriers and some other factors like defects increased. On the other hand, V_{oc} is maximum (2.39 V) at 2.5 eV because of optimized energy alignment and then decreases to minimum value of 2.03 V at 2.6 – 2.8 eV, possibly as a result of increased E_c offset. It also shows that P_{max} gradually rises from ~89.65 W (at 2.5 eV) to a maximum output ~112.79 W (at 2.8 eV) owing to this 2.8 eV, is signifying as ideal energy-alignments, lower energy loss during charge extraction, strong built-in electric field, enhanced electron injection into ETL, improved conduction band alignment with ETL and higher generation of charge carriers. Fig. 6(d) exhibits variation in %FF and %efficiency at different EA values, which illustrates that the FF increases continuously from 42.49% (at 2.5 eV) to a maximum magnitude of 63.01% (at 2.8 eV), suggesting a well balance between the photo generated carriers, and their collection at respective terminals with increasing EA. Probably, it further demonstrates that the optimum energy-level alignments increases carrier's transport and reduces recombination which ultimately cause efficiency to increase from ~8.96% (at 2.5 eV) to a peak of ~11.28% (at 2.8 eV). Of course, an EA of 2.5 eV yields an optimal V_{oc} of 2.39 V, a cut down V_{oc} of 2.03 V

View Article Online
DOI: 10.1039/D6MA00053C

result in the optimal efficiency at 2.8 eV. This noticeable disparity is caused by the trade-off involving carrier's transportation and increased in V_{oc}. A higher E_c mismatch within the device's boundaries enhances quasi-Fermi levels division as well V_{oc} at lowered EA to suppressing interfacial recombination. Nevertheless, this misalignment causes and extraction limitation, which raises resistive losses thus lowers FF. On the other hand, optimized alignment result from the EA of 2.8 eV, which promotes effective transportation of carriers, better carrier selectivity at interface, and lower energy loss during charge extraction and a greater FF. Therefore, the increase in FF exceeds the decrease in V_{oc}, leading to a higher total efficiency [46]. Table 5 provides the effect of BFO's EA variation on output characteristics of PV performance of proposed SCs configuration.

The photovoltaic success of several BFO-based solar cell topologies is summarized in the comparison Table 6, which shows a noticeable increase in efficiency with interfacial as well as transportation layers engineering improved. In consequence of restricted FF and carrier extraction, common FTO/BFO/Spiro-OMeTAD/Au modeled design displays poor efficiency (1.98%), highlighting the intrinsic recombination effects [47]. However, the efficiencies significantly rise when better aligned ETL layers are added, such as in ZnSe/BFO/Spiro-OMeTAD (10.73%) [48] and ZnO/BFO/GO (11.39%) constructed designs [49]. This enhancement is further increased in multi-layer structures like TiO_2/SnS/BFO/Spiro-OMeTAD, in which sequential energy alignment improves separation of carriers along with light absorption, leading to maximum theoretical efficiency (23.59%) [50]. On the other hand, ferroelectric heterostructures such as ITO/i-BFCO/n-Nb:STO exhibit relatively low efficiency (0.82%), indicating that transport constraints or suboptimal interfaces can't be compensated just by ferroelectric polarization only [51]. Whereas, concentrating on those experimentally recorded BFO-based structures, the performance behavior clearly demonstrates interfacial DOS along with charge transportation layer characteristics. The Graphite/BFO/ZnO/ITO/SLG exhibits the maximum efficiency (3.98%), mainly because of its modest FF (50.4%) and comparatively large J_{sc} (12.47 mA/cm^2) [52]. Additionally, due to its exceptionally low FF (0.39%) and J_{sc} (1.90 mA/cm^2), the NiO/BFTO/WS_2 structure exhibits inadequate efficiency (0.88%) and substantial interfacial losses [53]. Ultimately, the worst performance is seen regarding FTO/BFO/GO, in which ineffective transportation of carriers across the entire GO interface is confirmed by insignificant J_{sc} (0.134 mA/cm$^{2)}$ and efficiency (0.0207%) [54]. Furthermore, ITO/ZnO-uc/BFO/AI [27] and AI/BFO/ITO show substantially lower

View Article Online
DOI: 10.1039/D6MA00053C

efficiencies, suggesting increased junction selectivity together with reduced carrier extraction and greater recombination near metal contacts [55]. In the aforementioned settings, our suggested 3D ZnO/BFO/Spiro-OMeTAD configuration provides superior FF (64.91%) along with significant V_{oc} (1.8 V) to attain 11.83% efficiency. Consequently, the 3D ZnO/BFO/Spiro-OMeTAD architecture improves extrication of carriers along with optical absorption, demonstrating that interfacial settings along with nanostructured ETLs are essential for the advancement of BFO-based solar cells.

3.8 Resistance analysis

Fig. 7(a) illustrates the relationship b/w the series resistance (R_s), shunt resistance (R_{sh}), and characteristic resistance (R_{ch}) as the function of BFO layer thickness, varied from 300 to 1550 nm. The minimum Rs value (0.83 Ω-cm^2) is observed at lower BFO thickness, which can be attributed to reduced charge carrier recombination and the relatively low intrinsic resistivity of the BFO layer under optimized conditions. As the BFO thickness increases to 1550 nm, R_s progressively rises to 5.06 Ω-cm^2, primarily due to enhanced bulk recombination and the increased density of structural defects associated with thicker films. The R_{sh} reaches a maximum value of 1062 Ω-cm^2 at a BFO thickness of 550 nm, indicating minimal leakage pathways and suppressed interfacial recombination. However, further increasing the thickness results in a substantial decrease in R_{sh} to approximately 150 Ω-cm^2, which is attributed to the formation of interfacial defects and additional recombination centers that facilitate leakage currents. The overall R_{ch}, representing the combined influence of these resistive components, attains its maximum value (~26.96 Ω-cm^2) at a BFO thickness of 1550 nm, reflecting the cumulative effect of increased bulk and interfacial resistive losses.

Fig. 7(b) presents the dependence if R_s, R_{sh}, and R_{ch} on the thickness of ZnO. The minimum R_s value (4.28 Ω-cm^2) is observed at lower ZnO thickness, indicating reduced recombination losses and improved crystalline quality. As the ZnO layer thickness increases, R_s gradually increases to a maximum value of ~ 4.71 Ω-cm^2, which may be attributed to enhanced charge carrier recombination and increased structural imperfections. The highest R_{sh} value (~346 Ω-cm^2) is obtained at lower ETL thickness of ~10 nm, suggesting improved charge transport and minimized leakage pathways at reduced thickness. With further increases in ZnO thickness, R_{sh} decreased due to the increased probability of recombination and defect-assisted leakage. Similarly, the maximum

View Article Online
DOI: 10.1039/D6MA00053C

R_{ch} value (~24.38 Ω-cm^2) is observed at 10 nm ZnO thickness and subsequently declines as the ZnO layer becomes thicker, reflecting increased resistive losses in the device structure.

Fig. 7(c) describe the relationship b/w the DOS of BFO layer and the resistive parameters R_s, R_{sh}, and R_{ch}. At a DOS of 1×10^{18} 1/cm^3, R_s exhibits a relatively low value (~8.25 Ω-cm^2). However, as the DOS increases to 1×10^{20} 1/cm^3, R_s increases to ~9.76 Ω-cm^2 due to enhanced charge carrier recombination associated with a higher density of defect states. The maximum R_{sh} value (~1732 Ω-cm^2) is observed at a lower DOS of 1×10^{16} 1/cm^3, indicating suppresses leakage currents and minimal recombination. With increasing DOS, R_{sh} decreases significantly as additional defects states create conductive pathways that facilitate leakage currents and reduced overall device efficiency. The maximum R_{ch} value (~163.23 Ω-cm^2) occurs at a DOS of 1×10^{18} 1/cm^3, followed by a slight decline with further increases in DOS, reflecting the growing dominance of recombination-related resistive losses.

Fig. 7(d) illustrates the influence of BFO electron affinity of R_s, R_{sh}, and R_{ch}. The minimum R_s (~0.96 Ω-cm^2) is observed at an electron affinity of 2.6 eV, indicating favourable band alignment and efficient charge extraction. As the electron affinity increases, R_s rises to approximately 7.50 Ω-cm^2, which can be attributed to reduced carrier extraction efficiency and increased interfacial recombination. The maximum R_{sh} (~1372 Ω-cm^2) is achieved at moderated electron affinity values; however, as the electron affinity increases further to 2.8 eV, R_{sh} decreases to ~608 Ω-cm^2 due to enhanced recombination and leakage pathways. The highest R_{ch} (~24.38 Ω-cm^2) is observed at 2.5 eV, while a slightly lower value (~24.25 Ω-cm^2) is obtained near 2.7 eV, reflecting reduced electron and hole extraction efficiency at higher electron affinity values. Overall, these results demonstrate that both structural and electronic parameters critically influence the resistive behaviour and performance of the device.

4. Conclusion

In this study, a physically consistent three-dimensional ZnO/BFO/Spiro-OMeTAD perovskite solar cell architecture was investigated using COMSOL Multiphysics to identify the fundamental mechanisms governing device performance. The numerical analysis demonstrates that carrier transport and interface-assisted recombination losses, rather than limitations in bulk photogeneration, are the dominant factors restricting efficiency in BFO-based devices. This

View Article Online
DOI: 10.1039/D6MA00053C

mechanistic insight is supported by the observed sensitivity of device metrics to transport-layer and electronic-structure parameters across the multilayer stack.

The systematic variation of absorber thickness (300-1550 nm), density of states (1×10^{16}-1×10^{20} cm^{-3}), electron affinity (2.5-2.8 eV), and ETL thickness (10-60 nm) reveals that density of states engineering primarily controls open-circuit voltage and fill factor through its influence on recombination kinetics and quasi-Fermi level splitting. For instance, lower DOS values around 1×10^{16} cm^{-3} yielded improved voltage regulation and enabled efficiencies approaching 11.8%, confirming the critical role of defect-mediated recombination. Similarly, optimized band alignment at an electron affinity of approximately 1.8 eV enhanced carrier extraction and suppressed interfacial losses, resulting in a higher V_{oc} exceeding 2.0 V.

The absorber thickness optimization further indicates that a thinner BFO layer around 300 nm is sufficient to achieve efficient charge collection, yielding efficiencies of about 10.8% with $V_{oc} \approx 1.7$ V and $J_{sc} \approx 9.9$ mA cm^{-2}, while avoiding excessive recombination associated with thicker absorbers. In addition, ETL thickness was found to strongly affect series resistance and charge selectivity, with a thickness near 60 nm providing a favorable balance between transport efficiency and recombination suppression, leading to efficiencies above 11.8% and fill factors exceeding 65%.

Overall, these results demonstrate that performance enhancement in ZnO/BFO/Spiro-OMeTAD solar cells arises from physically meaningful control of interfacial transport and electronic structure rather than from numerical tuning alone. The coupled electrostatic and carrier-transport framework presented here provides transferable design guidelines for the experimental realization of stable, environmentally friendly, lead-free BFO-derived photovoltaic architectures.

References

[1] Alam, I., Mollick, R., and Ashraf, M. A. (2021). Numerical simulation of $Cs_2AgBiBr_6$-based perovskite solar cell with ZnO nanorod and P3HT as the charge transport layers. *Physica B: Condensed Matter*, *618*, 413187.

[2] Raj, A., Kumar, M., Kumar, A., Singh, K., Sharma, S., Singh, R. C., MS Pawar, MZA Yahya, Anshul, A. (2023). Comparative analysis of 'La'modified $BiFeO_3$-based perovskite solar cell devices for high conversion efficiency. *Ceramics International*, *49*(1), 1317-1327.

View Article Online
DOI: 10.1039/D6MA00053C

[3] Raza, M. A., Aman, M. M., Kumar, L., Al-Khasawneh, M. A., Faheem, M., and Ehyaei, M. A. (2025). Carbon neutrality and economic stability nexus: An integrated renewable energy transition to decarbonize the energy sector. *Energy Reports*, *13*, 4586-4608.

[4] Khadka, D. B., Sagadevan, S., Islam, M. A. U., Kato, S., and Soga, T. (2025). Photovoltaic Properties of Bismuth Vanadate/Bismuth Ferrite Heterostructures Prepared by Spin Coating. *Ceramics International*, *51*(1), 449-457.

[5] Muppana, V. N., Samykano, M., Pandey, A. K., Keng, N. W., Rajamony, R. K., and Suraparaju, S. K. (2025). Optimizing Charge Transport and Bandgap Alignment of ETL and HTL in Tin-Based Perovskite Solar Cells via Machine Learning. *Materials Today Communications*, 112874.

[6] Liang, J., Hu, X., Wang, C., Liang, C., Chen, C., Xiao, M., and Fang, G. (2022). Origins and influences of metallic lead in perovskite solar cells. *Joule*, *6*(4), 816-833.

[7] Pal, S., Sarath, N. V., Priya, K. S., and Murugavel, P. (2022). A review on ferroelectric systems for next generation photovoltaic applications. *Journal of Physics D: Applied Physics*, *55*(28), 283001.

[8] Zhu, P., Wang, D., Zhang, Y., Liang, Z., Li, J., Zeng, J and Xu, B. (2024). Aqueous synthesis of perovskite precursors for highly efficient perovskite solar cells. *Science*, *383*(6682), 524-531.

[9] Tan, J., Tong, S., Zhou, T., Lin, J., and Liu, Y. (2025). Research and development of modification strategies based on all inorganic perovskite solar cells. *Nano Energy*, *138*, 110815.

[10] De Jesús Bautista-Morantes, A., Calderón-Carvajal, C. O., Gómez-Cuaspud, J. A., and Vera-López, E. (2025). A new thin-film solar cell prototype based on Na-doped $BiFeO_3$. *Dyna*, *92*(237), 30-37.

[11] Pakravesh, F., and Izadyar, M. (2024). Theoretical insights into the electronic and optical properties of lithium-based perovskite for solar cell applications. *Journal of Photochemistry and Photobiology A: Chemistry*, *453*, 115602.

[12] Sunny, A., Rahman, S., Khatun, M., and Ahmed, S. R. A. (2021). Numerical study of high performance HTL-free $CH_3NH_3SnI_3$-based perovskite solar cell by SCAPS-1D. *AIP Advances*, *11*(6), 065102.

View Article Online
DOI: 10.1039/D6MA00053C

[13] Li, H., and Liu, S. (2024). Revolutionary SAMs: transforming inverted perovskite solar cells. *Journal of Materials Chemistry A*, *12*(17), 9929-9932.

[14] Mokgolo, P. J., Gumede, T. P., Ocaya, R. O., and Malevu, T. D. (2025). Enhancing Perovskite Solar Cells With Rare-Earth Metal Doped Zinc Oxide: A Review of Electron Mobility, Stability, and Photocarrier Recombination. *International Journal of Energy Research*, *2025*(1), 4240199.

[15] Qiu, C., Wu, Y., Song, J., Wang, W., and Li, Z. (2022). Efficient planar perovskite solar cells with ZnO electron transport layer. *Coatings*, *12*(12), 1981.

[16] Abdelkader E, Nadjia L, Naceur B, Favier Teodorescu L. (2022). Thermal, structural and optical properties of magnetic $BiFeO_3$ micron-particles synthesized by coprecipitation method: heterogeneous photocatalysis study under white LED irradiation. *Cerâmica*, *68*(385), 84-96.

[17] Renuka, H., Enaganti, P. K., Venkataraman, B. H., Ramaswamy, K., Kundu, S., and Goel, S. (2021). Submerged solar energy harvesting using ferroelectric Ti-doped BFO-based heterojunction solar cells. *International Journal of Energy Research*, *45*(14), 20400-20412.

[18] Khan, M. A., Shahbaz, K., Mustafa, G. M., Ramay, S. M., Naseem, S., and Atiq, S. (2023). Optimization of magnetoelectric coupling in $BiFeO_3$-$BaTiO_3$-$MnFe_2O_4$ tri-phase composites for ultra-sensitive devices. *Journal of Alloys and Compounds*, *947*, 169571.

[19] Carrasco-Hernández, A. R., Reyes-Rojas, A., Rojas-George, G., la Cruz, A. R. D., & Esparza-Ponce, H. E. (2025). Evaluation of Physical Properties of Ti-Doped $BiFeO_3$ Thin Films Deposited on Fluorine Tin Oxide and Indium Tin Oxide Substrates. *Materials*, *18*(10), 2395.

[20] Jalandhara, D., Kumar, S., Kumar, S., MM, R., Sharma, S. V., and Kaushal, S. (2025). $BiFeO_3$ as a Next-Generation Photocatalyst: Bridging Material Design with Environmental Remediation. *ChemPhysChem*, *26*(10), e202401092.

[21] Salman, M. U., Bilal, M., Karmani, Y. K., Ali, U., Ramay, S. M., Younis, M., and Atiq, S. (2025). Influence of acceptor/donor densities and layer thicknesses on the efficiency of 2D ZnO/BFO/spiro-OMeTAD perovskite solar cells: a COMSOL simulation-based optimization. *Journal of Materials Chemistry A*, *13*(20), 15057-15066.

View Article Online
DOI: 10.1039/D6MA00053C

[22] Kadim, G., Masrour, R., and Jabar, A. (2021). Ferroelectric, quantum efficiency and photovoltaic properties in perovskite $BiFeO_3$ thin films: first principle calculations and Monte Carlo study. *International Journal of Energy Research*, *45*(7), 9961-9969.

[23] Zhang, L., Liang, K. Y., Wang, Y. F., Hui, K. Z., Hu, T. Y., Yang, Z., and Zeng, J. H. (2025). Elevated Voltage on Sandwiched Semiconductor/Ferroelectric Photovoltaics. *ACS Applied Energy Materials*, *8*(5), 3096-3106.

[24] Shen, Y., Deng, K., and Li, L. (2022). Spiro-OMeTAD-Based Hole Transport Layer Engineering toward Stable Perovskite Solar Cells. *Small Methods*, *6*(11), 2200757.

[25] Cheng, M., Zuo, C., Wu, Y., Li, Z., Xu, B., Hua, Y., and Ding, L. (2020). Charge-transport layer engineering in perovskite solar cells. *Science Bulletin*, *65*(15), 1237-1241.

[26] Javed, A., Nasir, M. F., Azam, S., and Amin, M. A. (2025). Numerical simulation for a suitable electron transport layer of a lead-free $CuInSe_2$ based perovskite solar cell and PV module. *International Journal of Electrochemical Science*, *20*(1), 100893.

[27] Ceballos-Sanchez, O., Sanchez-Martinez, A., Flores-Ruiz, F. J., Huerta-Flores, A. M., Torres-Martínez, L. M., Ruelas, R., and García-Guaderrama, M. (2020). Study of $BiFeO_3$ thin film obtained by a simple chemical method for the heterojunction-type solar cell design. *Journal of Alloys and Compounds*, *832*, 154923.

[28] Wani, W. A., Gupta, G., Rath, S., Venkataraman, H., and Ramaswamy, K. (2024). Photon upconversion assisted ferroelectric photovoltaics: Device configuration with multifaceted influence in augmenting the photovoltaic response of $BiFeO_3$ thin-film solar cells. *Progress in Photovoltaics: Research and Applications*, *32*(8), 556-568.

[29] Afzal, A. M., Javed, Y., Hussain, S., Ali, A., Yaqoob, M. Z., and Mumtaz, S. (2020). Enhancement in photovoltaic properties of bismuth ferrite/zinc oxide heterostructure solar cell device with graphene/indium tin oxide hybrid electrodes. *Ceramics International*, *46*(7), 9161-9169.

[30] Raj, A., Sharma, S., Singh, D. V., Kumar, A., Chourasia, R. K., Siqueiros, J. M., Herrera, O.R., Anshul, A., and Kumar, M. (2024). Photovoltaic energy conversion in multiferroic

View Article Online
DOI: 10.1039/D6MA00053C

perovskite absorber-based devices via experiment and theoretical calculations. *Physica B: Condensed Matter*, *673*, 415504.

[31] Mahammedi, N. A., Benameur, A., Gueffaf, H., Merabet, B., Ozkendir, O. M., and Sato, S. I. (2024). Investigating a Pb-free nip perovskite solar cell with BFCO absorber using SCAPS-1D. *Optik*, *302*, 171659.

[32] Abedini-Ahangarkola, H., and Soleimani-Amiri, S. (2021). Design and analysis of high efficiency perovskite solar cells with light trapping nano-textured substrates. *International Journal of Engineering*, *34*(4), 873-880.

[33] Makableh, Y. F., Hassan, W., Awad, I. A., and Aljaiuossi, G. (2021). Comprehensive Electrical modeling analysis of Heterojunction Perovskite Solar Cells by using different electron transport nanostructured layers. *Superlattices and Microstructures*, *150*, 106777.

[34] Elewa, S., Yousif, B., and Abo-Elsoud, M. E. A. (2021). Improving efficiency of perovskite solar cell using optimized front surface nanospheres grating. *Applied physics A*, *127*, 1-14.

[35] Zandi, S., Saxena, P., and Gorji, N. E. (2020). Numerical simulation of heat distribution in RGO-contacted perovskite solar cells using COMSOL. *Solar Energy*, *197*, 105-110.

[36] Mohammadi, M. H., Eskandari, M., and Fathi, D. (2023). Morphological investigation and 3D simulation of plasmonic nanostructures to improve the efficiency of perovskite solar cells. *Scientific Reports*, *13*(1), 18584.

[37] Wang, Z. Q., Xiong, Z. H., Hu, W. J., Jiang, J. J., Cheng, Z. B., Xue, Y. M., Peng, L., and Lin, J. (2025). Exploration of Double Perovskite Material Space via Machine Learning for Tandem Solar Cells. *Acta Physica Polonica A*, *147*(6), 488-488.

[38] Kenfack, G. M. D., Nya, F. T., and Laref, A. (2024). Organic solar cell efficiency improvement through architecture engineering by integrating carbon nanoring–SCAPS 1D modelling. *Materials Chemistry and Physics*, *324*, 129713.

[39] Karimi, E., Ghorashi, S. M. B., and Hashemi, M. (2020). Optical and Elecrtical Simulation of $CH_3NH_3PbI_3$-based Perovskite Solar Cells. *International Journal of Optics and Photonics*, *14*(1), 57-66.

View Article Online
DOI: 10.1039/D6MA00053C

[40] Bhattarai, S., Hossain, M. K., Madan, J., Pandey, R., Samajdar, D. P., Ansari, M. Z., and Amami, M. (2024). Performance improvement of HTL-free perovskite solar cells with the graded approach by numerical simulation. *Journal of Physics and Chemistry of Solids*, *184*, 111691.

[41] Clarke, W., Wolf, M. J., Walker, A., and Richardson, G. (2023). Charge transport modelling of perovskite solar cells accounting for non-Boltzmann statistics in organic and highly-doped transport layers. *Journal of Physics: Energy*, *5*(2), 025007.

[42] Cheng, W., Liu, Y., Zhou, R., Yang, Y., Wang, C., Li, Y., and Chen, L. (2024). Exploring Optoelectronic-Thermal Coupling in Perovskite Solar Cells Utilizing Varied Hole Transport Layers. *Advanced Theory and Simulations*, *7*(3), 2300749.

[43] Karmani, Y. K., Bilal, M., Salman, M. U., Ameen, M., Luqman, M., Ramay, S. M., and Atiq, S. (2025). Correlation between trap-assisted non-radiative recombination losses and thermal agitation in SnS-based solar cell: A state-of-the-art computational analysis. *Materials Science and Engineering: B*, *321*, 118484.

[44] Zhou, R., Chen, Y., Zhou, L., Yao, Y., Liu, Y., Wang, C., and Chen, L. (2024). Inhibiting hysteresis and optimizing the performance of perovskite solar cells. *Solar Energy Materials and Solar Cells*, *264*, 112616.

[45] Nkele, A. C., Ike, I. S., Ezugwu, S., Maaza, M., and Ezema, F. I. (2021). An overview of the mathematical modelling of perovskite solar cells towards achieving highly efficient perovskite devices. *International Journal of Energy Research*, *45*(2), 1496-1516.

[46] Rehman, U. U., Sahar, K. U., Hussain, E., and Wang, C. M. (2024). Performance optimization of lead-free potassium germanium halide based perovskite solar cells: A numerical study. *Solar Energy*, *277*, 112752.

[47] Huang, L. (2023). Relating band edge DOS occupancy statistics associated excited state electron entropy generation to free energy loss and intrinsic V_{oc} deficit of solar cells. *Physical Chemistry Chemical Physics*, *25*(20), 14334-14347.

[48] Mudassar, M. M., Arshad, M., Salman, M. U., Mahmood, A., Al-Masry, W., Asim, M., & Atiq, S. (2025). Significance of the direct relation between the fill factor and hole transport layer thickness in perovskite-based solar cells for green energies. *RSC Advances*, *15*(40), 33830-33843.

View Article Online
DOI: 10.1039/D6MA00053C

[49] Soucase, B. M., Baig, F., Khattak, Y. H., Vega, E., and Mollar, M. (2022). Numerical analysis for efficiency limits of experimental perovskite solar cell. *Solar Energy*, *235*, 200-208.

[50] Beepat, K. G., Sharma, D. P., Mahajan, A., Pathak, D., and Kumar, V. (2024). Simulation of multijunction solar cell interfaces for enhancement of the power conversion efficiency. *Discover Applied Sciences*, *6*(6), 1-19.

[51] Raza, E., Bhadra, J., Asif, M., Aziz, F., Al-Thani, N. J., and Ahmad, Z. (2023). A numerical approach to study the effect of bandgap and electron affinity in HTL-free perovskite solar cells and design of two-terminal silicon/perovskite tandem solar cell. *Materials Today Communications*, *37*, 107383.

[52] Alsalme, A., Altowairqi, M. F., Alhamed, A. A., and Khan, R. A. (2022). Optimization of photovoltaic performance of Pb-free perovskite solar cells via numerical simulation. *Molecules*, *28*(1), 224.

[53] Salman, M. U., Mehak, M., Ali, U., Din, G. M. U., Ramay, S. M., Younis, M., and Atiq, S. (2025). Direct correlation between open-circuit voltage and quasi-fermi level splitting in perovskite solar cells: a computational step involving thickness, doping, lifetime, and temperature variations for green solutions. *RSC Advances*, *15*(20), 15618-15629.

[54] Mustafa, G. M., Younas, B., Saba, S., Elqahtani, Z. M., Alwadai, N., and Aftab, S. (2024). Numerical simulation to optimize power conversion efficiency of an FTO/GO/$Cs_2AgBiBr_6$/Cu_2O solar cell. *RSC Advances*, *14*(27), 18957-18969.

[55] Wani, W. A., Renuka, H., Kundu, S., Goel, S., Venkataraman, H., & Ramaswamy, K. (2022). What ails the photovoltaic performance in single-layered unpoled BFO?–The role of oxygen annealing in improving the photovoltaic efficiency. *Solar Energy*, *236*, 822-831.

View Article Online
DOI: 10.1039/D6MA00053C

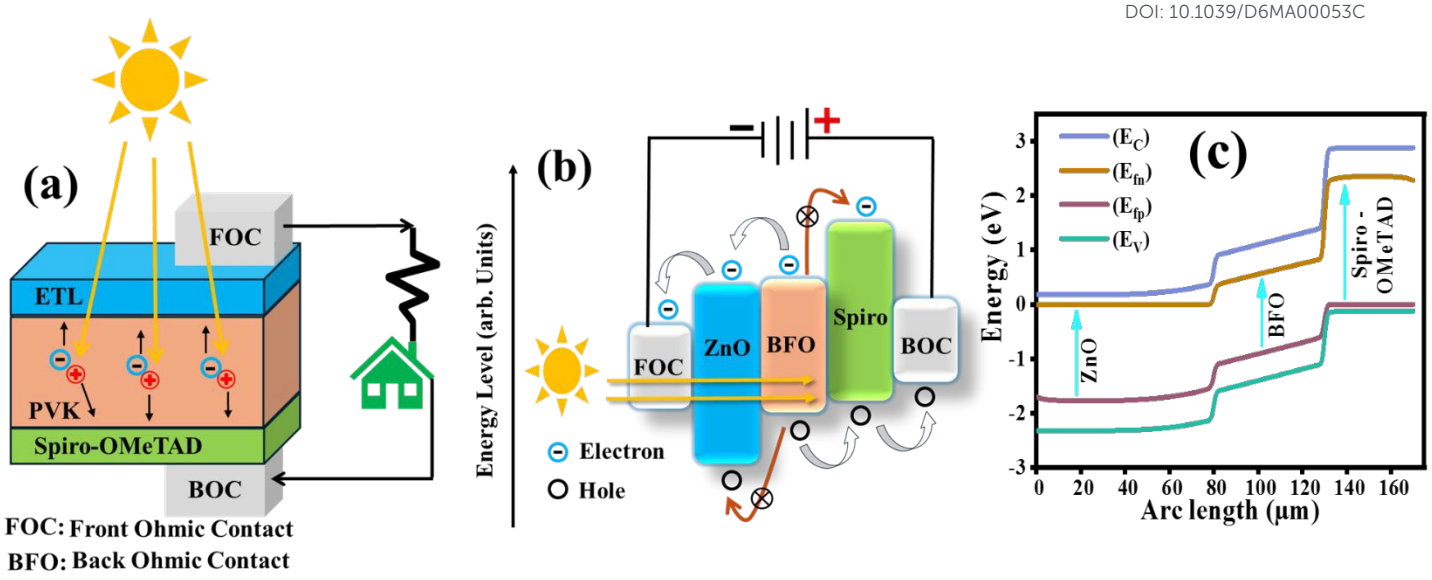

Figure 1(a) Solar cell's schematic diagram of ZnO/BFO/Spiro-OMeTAD architecture, **(b)** schematic with arbitrary energy levels to show the available paths for electrons and holes, and **(c)** energy band diagram under illumination as a function of arc length

View Article Online
DOI: 10.1039/D6MA00053C

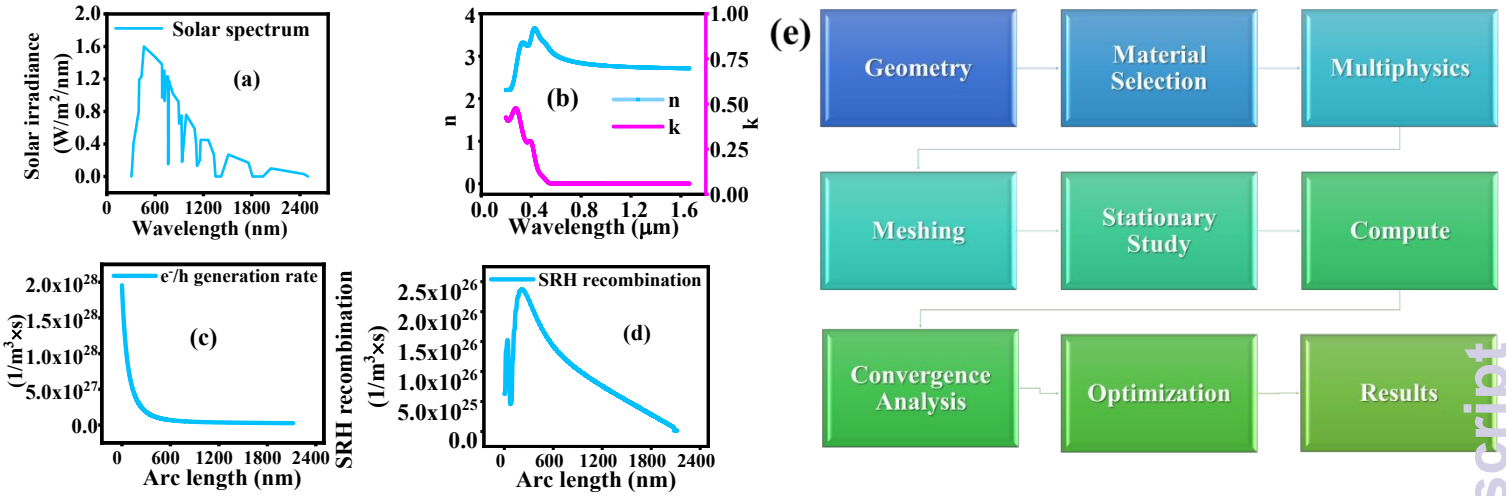

Figure 2(a) Solar spectrum AM 1.5G, **(b)** variation of refractive index and extinction coefficient (n,k) with respect to wavelength, **(c)** electron/hole generation rate as a function of arc length, **(d)** Shockley-Read-Hall (SRH) recombination as a function of arc length, and **(e)** schematic flowchart, highlighting the essential steps for device building

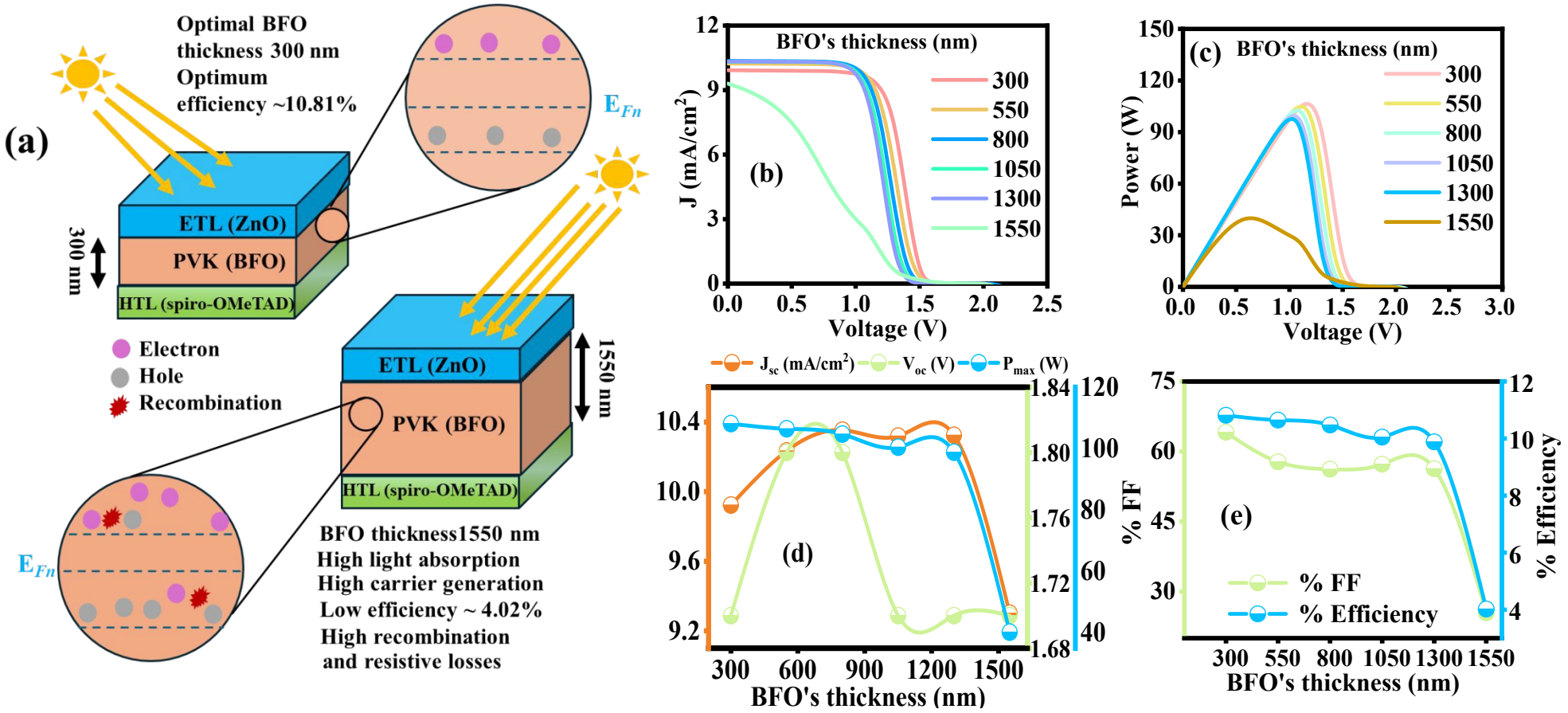

Figure 3(a) Schematic illustration of solar cell working, highlighting the role of BFO's thickness variation on; **(b)** J-V curve, **(c)** P-V curve of 3D ZnO/BFO/Spiro-OMeTAD solar cell and effect of BFO's thickness variation on **(d)** J_{sc}, V_{oc}, and P_{max}, and **(e)** %FF, and %Efficiency with respect to BFO's thickness variation

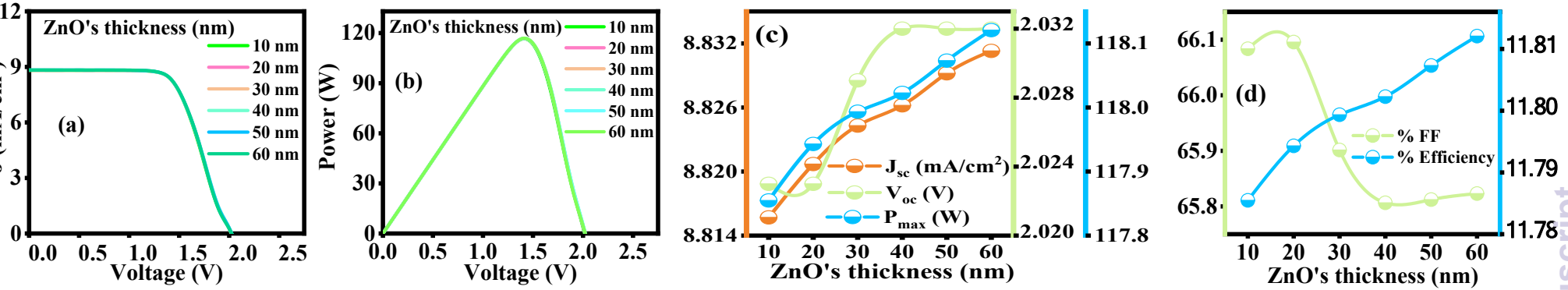

Figure 4(a) J-V curves, **(b)** P-V curves for varied ZnO thicknesses in 3D ZnO/BFO/Spiro-OMeTAD solar cell and their effects on **(c)** J_{sc}, V_{oc}, and P_{max}, and **(d)** %FF, and %Efficiency

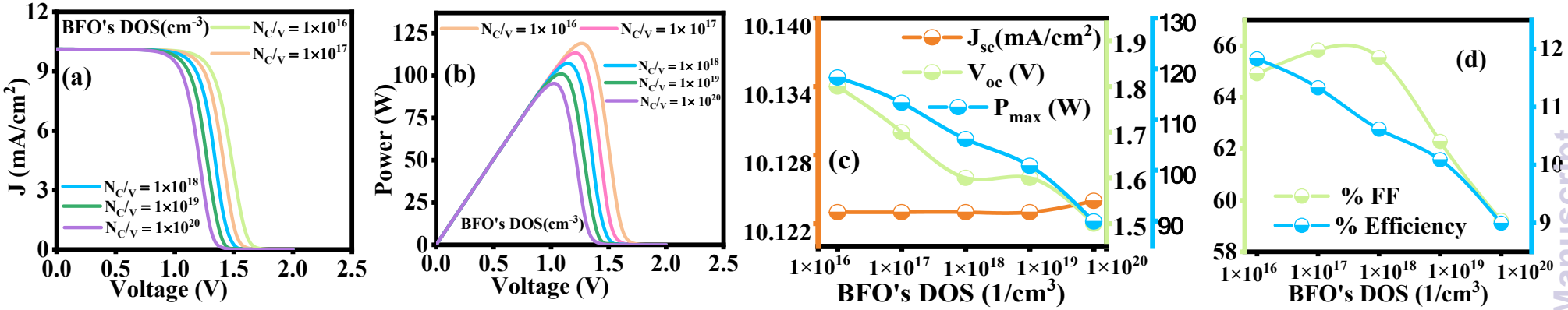

Figure 5(a) J-V curves, **(b)** P-V curves for varied BFO's conduction (N_c) & valence band (N_v) density of states (DOS) in 3D ZnO/BFO/Spiro-OMeTAD solar cell and their effects on **(c)** J_{sc}, V_{oc}, and P_{max}, and **(d)** %FF, and %Efficiency

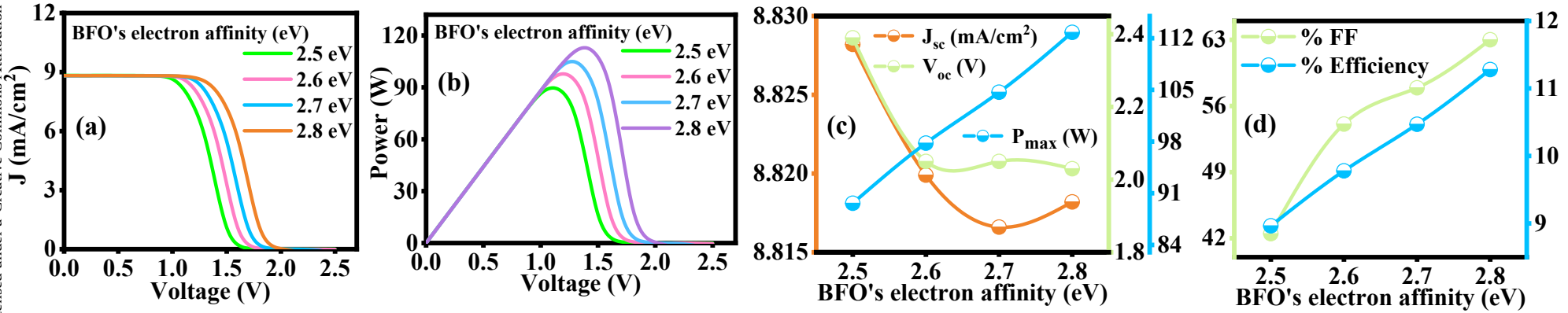

Figure 6(a) J-V curves, **(b)** P-V curves for varied BFO's electron affinity in 3D ZnO/BFO/Spiro-OMeTAD solar cell and their effects on **(c)** J_{sc}, V_{oc}, and P_{max}, and **(d)** %FF, and %Efficiency

View Article Online
DOI: 10.1039/D6MA00053C

Table 1 Basic input optimized parameters of each layer in 3D ZnO/BFO/Spiro-OMeTAD PSC

Material properties	ZnO	BFO	Spiro-OMeTAD
Relative permittivity	6	6	3
Band gap (eV)	2.5	2.5	3
Electron affinity (eV)	3.8	2.8	1.9
Effective DOS valence band (cm^{-3})	1×10^{20}	5×10^{18}	1×10^{20}
Effective DOS conduction band (cm^{-3})	1×10^{20}	5×10^{18}	1×10^{20}
Electron mobility ($cm^2/V.s$)	150	80	2
Hole mobility ($cm^2/V.s$)	25	25	1×10^{-2}
Electron lifetime, SRH (ns)	1	1000	1
Hole lifetime, SRH (ns)	1	1000	1

Table 2 Designed structure (3D ZnO/BFO/Spiro-OMeTAD) output performance parameters with varying BFO's thickness

BFO's thickness (nm)	J_{sc} (mA/cm^2)	V_{oc} (V)	P_{max} (W)	FF %	Efficiency %
300	9.92	1.7	108.14	64.11	10.81
550	10.23	1.8	106.46	57.79	10.65
800	10.35	1.8	104.73	56.20	10.47
1050	10.32	1.7	100.47	57.28	10.05
1300	10.32	1.7	98.82	56.31	9.88
1550	9.30	1.7	40.24	25.45	4.02

Table 3 Designed architecture (3D ZnO/BFO/Spiro-OMeTAD) performance parameters with varying ZnO's thickness

ZnO's thickness (nm)	J_{sc} (mA/cm^2)	V_{oc} (V)	P_{max} (W)	FF %	Efficiency %
10	8.82	2.02	117.85	66.08	11.785
20	8.82	2.02	117.94	66.10	11.794
30	8.82	2.03	117.99	65.90	11.799
40	8.83	2.03	118.02	65.81	11.802
50	8.83	2.23	118.07	65.81	11.807
60	8.83	2.03	118.12	65.82	11.812

View Article Online
DOI: 10.1039/D6MA00053C

Table 4 Designed architecture (3D ZnO/BFO/Spiro-OMeTAD) performance parameters with varying density of states (DOS) in conduction and valence band (N_c, N_v) of BFO layer

N_c and N_v (cm^{-3})	J_{sc} (mA/cm^2)	V_{oc} (V)	P_{max} (W)	FF %	Efficiency %
1×10^{16}	10.123	1.8	118.28	64.91	11.83
1×10^{17}	10.123	1.7	113.30	65.83	11.33
1×10^{18}	10.123	1.6	106.15	65.54	10.62
1×10^{19}	10.123	1.6	100.88	62.28	10.09
1×10^{20}	10.124	1.5	89.93	59.22	8.99

Table 5 Designed structure (3D ZnO/BFO/Spiro-OMeTAD) performance parameters with varying electron affinity (EA) of BFO layer

EA (eV)	J_{sc} (mA/cm^2)	V_{oc} (V)	P_{max} (W)	FF %	Efficiency %
2.5	8.83	2.39	89.65	42.49	8.96
2.6	8.82	2.05	97.79	54.08	9.78
2.7	8.82	2.05	104.69	57.92	10.47
2.8	8.82	2.03	112.79	63.01	11.28

Table 6 Comparative analysis of the physical parameters of various BFO-based simulation and experimental device structures for efficient solar cell design

Solar cell structure	J_{sc} (mA/cm^2)	V_{oc} (V)	FF %	Efficiency %	Ref.
FTO/BFO/Spiro-OMeTAD/Au (simulation)	8.35	0.79	29.10	1.92	[47]
ZnSe/BFO/Spiro-OMeTAD (simulation)	8.83	1.96	61.91	10.73	[48]
ZnO/BFO/GO (simulation)	8.93	2.21	71.47	11.39	[49]
TiO_2/SnS/BFO/Spiro-OMeTAD (simulation)	29.83	0.95	82.83	23.59	[50]
ITO/i-BFCO/n-Nb:STO (simulation)	4.0	0.41	49.8	0.82	[51]
Graphite/BFO/ZnO/ITO/SLG (experimental)	12.47	0.642	50.4	3.98	[52]
ITO/ZnO-uc/BFO/AI (experimental)	4.7	0.89	53	2.21	[28]
NiO/BFTO/WS_2 (experimental)	1.90	0.8	0.39	0.88	[53]
FTO/ BFO/GO (experimental)	0.134	0.33	46.87	0.0207	[54]
AI/BFO/ITO (experimental)	2.34	0.92	37	0.89	[55]
3D ZnO/BFO/Spiro-OMeTAD	10.12	1.8	64.91	11.83	This work

View Article Online
DOI: 10.1039/D6MA00053C

Data Availability Statement

The data will be available on request.